Materials Research Proceedings **32** (2023) 244-252 https://doi.org/10.21741/9781644902615-28

Hot deformation of ultrafine-grained TiC-reinforced AlCrFeNbMoTiV refractory high entropy alloys

P. Martin[1,a*], C. Aguilar[2,b], B. Ferrari[3,c], A.J. Sánchez-Herencia[3,d], J.M. Cabrera[1,4,e]

[1]Deparment of Materials Science and Engineering EEBE, Technical University of Catalonia, c/Eduard Maristany 10-14, 08019 Barcelona, Spain

[2]Department of Materials and Metallurgical Engineering, Technical University Federico Santa María, Av. España 1680, 2340000 Valparaíso, Chile

[3]Institute of Glass and Ceramics ICV-CSIC, c/Kelsen 5, 28049 Madrid, Spain

[4]Fundació CIM-UPC, c/Llorens i Artigas 12, 08028 Barcelona, Spain

[a]pablo.martin.saint-laurence@upc.edu, [b]claudio.aguilar@usm.cl, [c]bferrari@icv.csic.es, [d]ajsanchez@icv.csic.es, [e]jose.maria.cabrera@upc.edu

Keywords: Constitutive Equation, High-Entropy Alloys, Complex Concentrated Alloys, Ultrafine-Grained, Mechanical Properties

Abstract. In the present work, the hot deformation behavior of the $AlCr_{0.2}FeNbMoTiV_2$ refractory high-entropy alloy was studied by means of its constitutive modeling. The samples were fabricated using mechanical alloying and spark plasma sintering, resulting in an ultrafine-grained microstructure consisting of a main bcc solid solution, Laves phase, and TiC and Al_2O_3 precipitates. Compression tests between 950 and 1100 ºC and $5\cdot10^{-4}$ and 10^{-2} s^{-1} of strain rate were performed in order to determine the constitutive equations. Additionally, the samples were subjected to a heat treatment at 1350 ºC for 16 h, presenting a considerable increment in the specific yield strength (from 33 to 94 $MPa\cdot g^{-1}\cdot cm^3$ at 1000 ºC) accompanied by a slight increase of the grain size (from 0.35 to 1.2 μm). Overall, the heat-treated $AlCr_{0.2}FeNbMoTiV_2$ alloy presented one of the highest specific yield strength values among refractory high entropy alloys.

Introduction

The current challenges of the aerospace industry require advanced materials that can overcome the performance of current materials in terms of high-temperature strength and oxidation resistance, among others. Among the potential candidates to fulfill these requirements, refractory high-entropy alloys (RHEAs), first proposed in 2010 [1,2], have attracted the interest of the scientific community because of their outstanding performance in terms mechanical properties at elevated temperatures (even superior to that of commercial Ni-based superalloys) and elevated oxidation resistance [3]. As part of the high-entropy alloys (HEAs) family, these materials correspond to multicomponent alloys (typically over five) with contents between 5 and 35 at. pct., resulting in complex compositions far away from the boundaries of the traditional alloy design concept. RHEAs, particularly, are mainly constituted by refractory elements (like Mo, Nb, Ta, or W) that provide elevated hot softening resistance, alloyed with non-refractory elements (like Al, Si, or Fe) that reduce the density or enhance oxidation resistance properties. Even though RHEAs are commonly fabricated by casting techniques, the mechanical alloying (MA) followed by spark plasma sintering (SPS) route has proven to produce the strongest RHEAs because of the combination of fine or ultrafine grains and the formation of finely and homogeneously dispersed oxides and nitrides [4,5]. This particular microstructure results in superior properties at high temperatures and a superior balance of strength and ductility at room temperature [6,7].

Materials Research Proceedings **32** (2023) 244-252 https://doi.org/10.21741/9781644902615-28

The constitutive analysis of the high-temperature deformation of metallic materials can result not only in an accurate description of the effect of temperature and strain rate over the flow stress but it also provides insightful details about the deformation and softening mechanisms involved. Several expressions have been proposed for these purposes. One of them, the power law (Eq. 1), relates the Zenner-Hollomon (Z) parameter (defined as the temperature-compensated strain rate) with the stress, particularly in low-stress conditions (high temperatures and low strain rates) [8].

$$Z = \dot{\varepsilon} \exp\left(\frac{Q_{app}}{RT}\right) = A'\sigma^{n'} \quad (1)$$

where Q_{app} corresponds to the apparent activation energy, $\dot{\varepsilon}$ to the strain rate, R to the gas constant, T to the temperature, and A' and n' are parameters of the model.

To the authors' knowledge, this is the first work that addresses the constitutive modeling of a PM-fabricated RHEA, resulting in an expression that accurately predicts the peak stress (σ_P) between 1000 – 1100 ºC and 0.0005 – 0.01 s^{-1}. Additionally, the physical meaning of n' and Q_{app} was discussed in order to contribute to the comprehension of the deformation mechanisms of RHEAs with typical microstructural features of powder metallurgy processing. Lastly, the effect of annealing on the alloy's microstructure and high-temperature mechanical properties was evaluated.

Materials and methodologies

The powder alloy (denominated R2) was produced mixing pure commercial powders of Al (< 45 µm, 99.5%), Cr (< 45 µm, 99%), Mo (3-7 µm, 99.95%), Nb (< 45 µm, 99.8%), Ti (< 45 µm, 99%), and V (<45 µm, 99.5%), employing hardened steel vials and balls which can act as a source of Fe. The milling process was conducted in a high-energy planetary ball mill Fritsch Pulverisette 5, for 50 h, using a ball-to-powder ratio (BPR) of 20:1 and 300 rpm of rotational speed under an Ar atmosphere. Additionally, 2.6 wt. pct. of ethylene bis-stereamide was added as a Process Control Agent (PCA), and on/off cycles of 30 min/30 min were utilized to avoid severe cold welding. Table 1 summarizes the composition of the 50 h-milled powder used in the sintering stage. The SPS was conducted in a Dr. Sinter SPS-1050-CE press, using 1150 ºC and 50 MPa of stress, with a dwell time of 10 min in vacuum. Disks of 30 mm in diameter and between 8 and 9 mm in height were sintered using graphite die and punches. As-sintered samples (R2AS) were subjected to an annealing treatment at 1350 ºC for 16 h under an Ar atmosphere (R2HT).

Table 1: Composition of the Mechanically Alloyed (MA-ed) R2 powder.

Al (at. pct.)	Cr (at. pct.)	Fe (at. pct.)	Mo (at. pct.)	Nb (at. pct.)	Ti (at. pct.)	V (at. pct.)
12.49	4.67	13.63	14.48	14.36	13.66	26.72

X-ray diffraction (XRD) analysis was performed in a Bruker D8 Advance diffractometer, using $Cu_{k\alpha 1}$-radiation (λ = 0.15406 nm) equipped with a Ge monochromator. Besides, transmission electron microscopy (TEM) was performed employing a J2100F microscope equipped with energy-dispersive X-ray spectroscopy (EDS) detector. For these purposes, a lamella was prepared in a Focus Ion Beam (FIB)-SEM Neon40 Crossbeam™ workstation. A field-emission gun SEM JEOL JSM-7001F equipped with EDS and electron backscattered diffraction (EBSD) detectors was also used, utilizing the MTEX package to process the EBSD data. Lastly, 6 mm in diameter and 8 mm in height cylindrical samples were cut from the sintered samples for compression testing. Tests at different temperatures (950, 1000, 1050, and 1100 ºC) and different strain rates (0.0005, 0.001, 0.005, and 0.01 s^{-1}) were performed in an Instron 4507 universal testing machine equipped with a load cell of 100 kN, using Ar flow to avoid oxidation of the samples, and a layer of mica and boron nitride to diminish the friction between the samples and the punches.

Materials Research Proceedings **32** (2023) 244-252 https://doi.org/10.21741/9781644902615-28

Results and discussion

According to the XRD analysis (Figure 1), both R2AS and R2HT samples are mainly constituted by a bcc phase with lattice parameters similar to that of V, TiC, and Laves phases (C14 and C36 polytypes observed in both samples, while minor C15 was observed in R2AS too). Additionally, in the case of the R2HT sample, Al_2O_3 peaks were observed. Figure 2.a and Figure 2.d illustrates the microstructure of R2AS and R2HT, respectively, evidencing fully-dense microstructures. According to the respective EDS mapping images (Figure 2.b and Figure 2.e), both samples exhibited the same elemental distribution: a V, Mo-rich solid solution, the Ti, Nb-rich carbide, the Fe, Nb-rich Laves phases, and minor Al_2O_3 particles. According to the image analysis performed over the microstructure images, the bcc phase reaches over 45 pct. of the area, while carbides are around 25 pct. In the same way, Figure 2.c and Figure 2.f depicts the Inverse Pole Figure (IPF) map of the respective samples, showing the orientation of the bcc and fcc grains. The average grain size of the bcc and carbide phases of the R2AS sample is around 0.35 and 0.25 µm which increases to 1.3 and 1.1 µm in the R2HT sample, respectively. Apart from that, no remarkable changes in phase equilibrium or composition were observed.

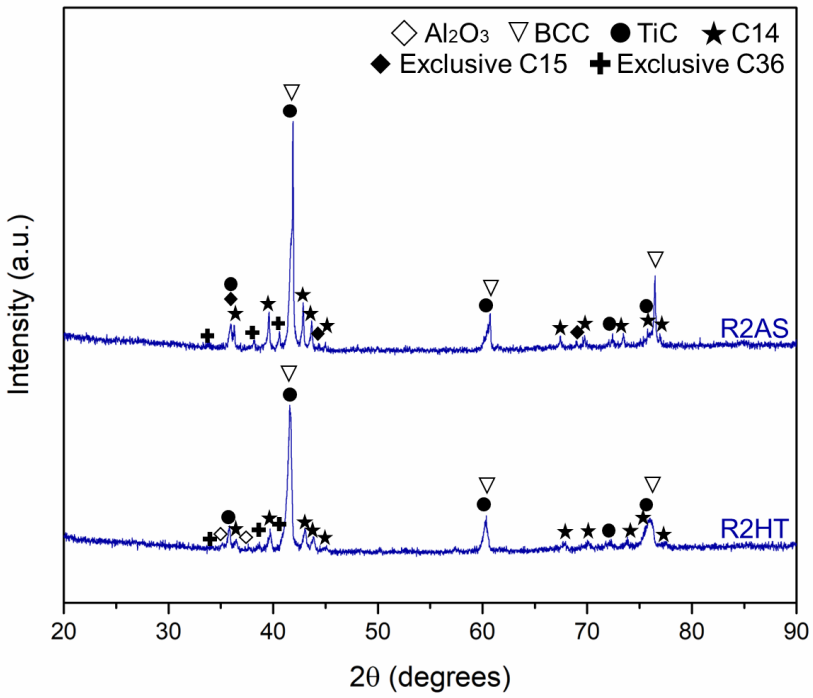

Figure 1: XRD pattern of R2AS and R2HT.

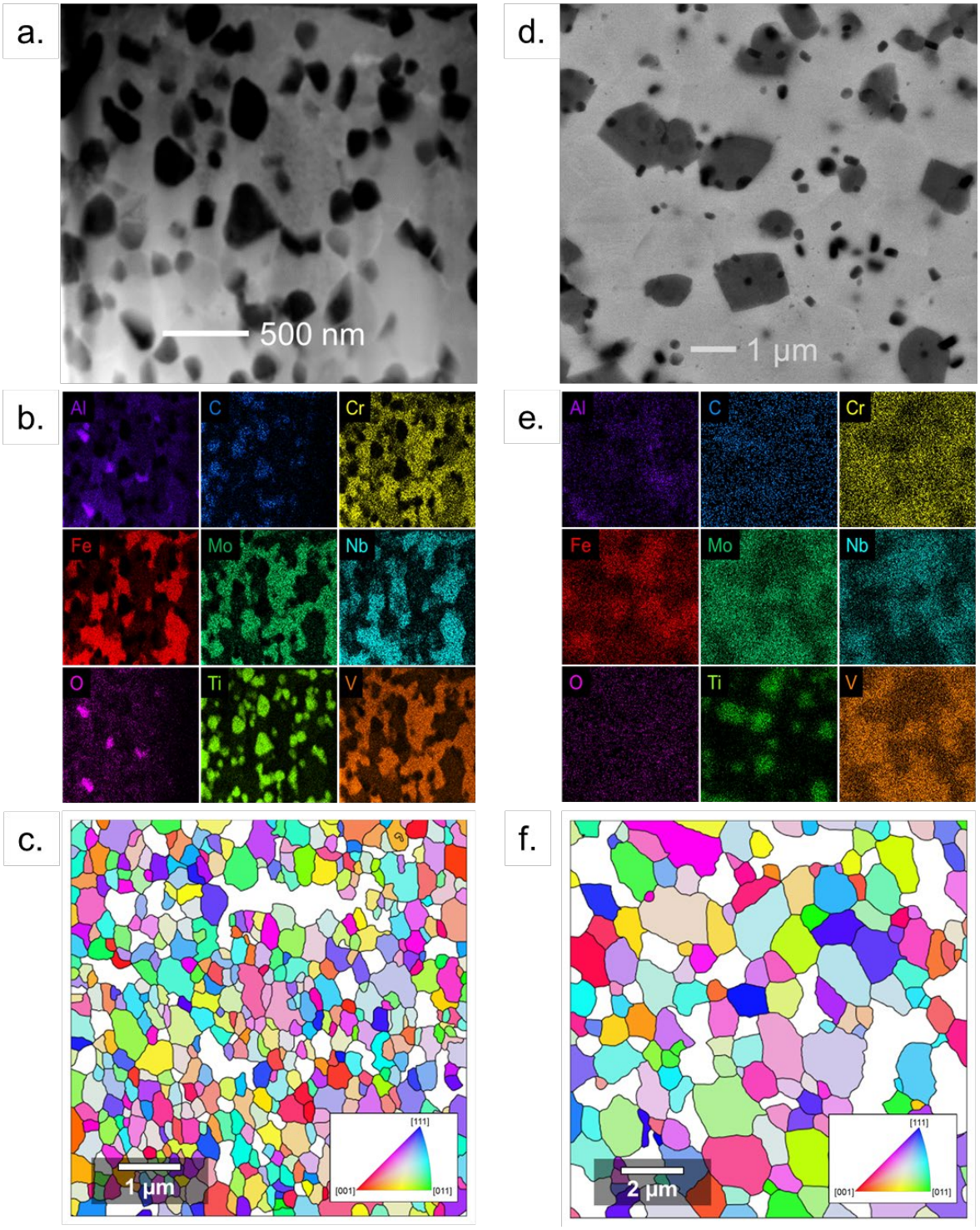

Figure 2: a) TEM image of R2AS microstructure; b) EDS mapping images of the region showed in a; c) IPF map of bcc and fcc grains subset of R2AS; d) SEM image of R2HT microstructure; e) EDS mapping images of the region showed in d; and f) IPF map of bcc and fcc grains subset of R2HT.

Figure 3 presents the compression curves of the R2AS samples at different temperatures and strain rates. The material exhibited the typical behavior of metallic materials: increasing the temperature or decreasing the strain rate reduces the flow stress. Apart from that, the shape of the curves obtained at 1100 and 1050 ºC indicates the predominance of dynamic recovery (DRV) as the softening mechanism. In opposition, curves obtained at high strain rates at 1000 ºC and at low

Materials Research Proceedings **32** (2023) 244-252 https://doi.org/10.21741/9781644902615-28

strain rates at 950 ºC suggest that dynamic recrystallization (DRX) may have predominated instead. It is also important to highlight that a strain of 0.7 was achieved in most cases, except for those tests at 950 ºC using strain rates of 0.005 and 0.01 s^{-1}. In those samples, some cracks appeared during the elastic deformation region, indicating that the material was already brittle, which resulted in scarce ductility. Additionally, there is a considerable difference in the peak stresses (σ_P) obtained at 1000 ºC and 950 ºC at 0.001 and 0.0005 s^{-1}. All these findings suggest that the mechanical behavior changes in that temperature interval, either by dissolution/precipitation phenomena or a change in the controlling deformation mechanism. For the previous reasons, the constitutive analysis will be performed only considering the 1000-1100 ºC range.

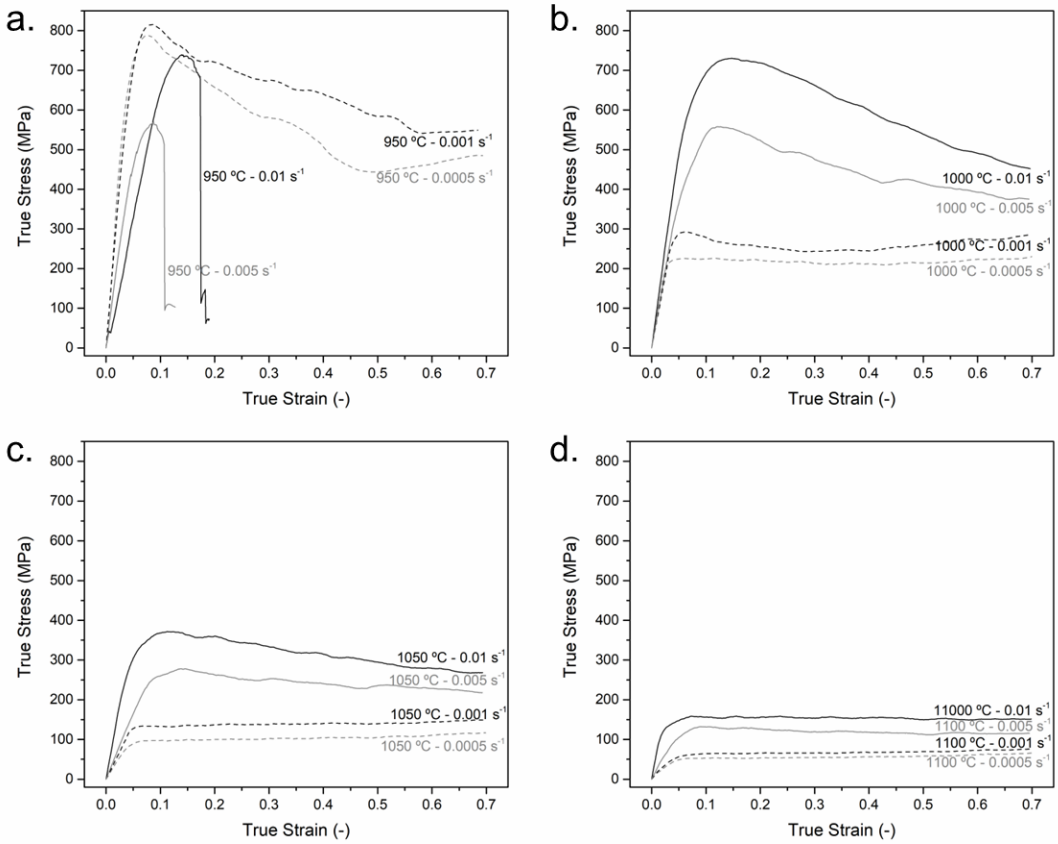

Figure 3: Compression curves of the R2AS samples at different strain rates and at a) 950 ºC, b) 1000 ºC, c) 1050 ºC, and d) 1100 ºC.

Figure 4.a illustrates the linear relationship between ln $\dot{\varepsilon}$ and ln σ_P as described in Eq. 2. The slopes of the curves of each plot correspond to n', resulting in values of 2.60, 2.23, and 2.54, at 1100, 1050, and 1000 ºC, respectively, resulting in an average n' value of 2.46. The excellent R^2 values, as well as the similarity between the calculated n' values, confirm that there is no change in the deformation mechanism in the range of study. According to the literature, n' = 2 is associated with grain-boundary sliding (GBS) as the governing deformation mechanism. This is the typical deformation mechanism of ultrafine-grained materials, and it has been reported in several works contributing to the hot deformation of PM-fabricated RHEAs or in the recrystallized grains of coarse-grained RHEAs [9,10]. In the present analysis, the obtained n' value is slightly superior to the theoretical one of GBS. Nevertheless, it has been described that in multi-phase materials, the n' value obtained by means of the constitutive analysis is superior to the actual value; the load is actually distributed between two or more phases, and therefore, the stress actually exerted over the

Materials Research Proceedings **32** (2023) 244-252 https://doi.org/10.21741/9781644902615-28

matrix phase is inferior to the experimental measured one [11]. Hence, the rest of the analysis considers n' = 2.

$$\ln \dot{\varepsilon} + Q_{app}/R(1/T) = \ln A^{'} + \mathrm{n}^{'} \ln \sigma_P \quad (2)$$

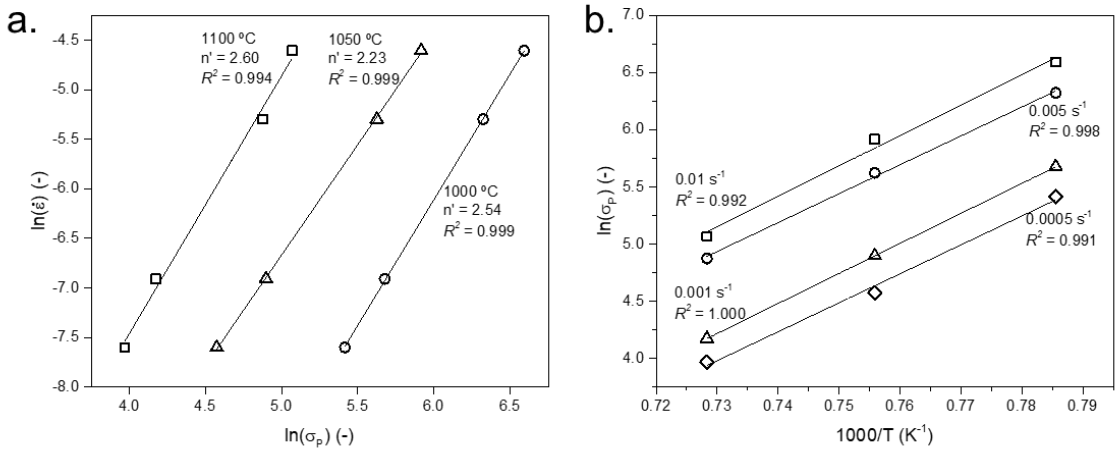

Figure 4: Plots used to determine the values of a) n' and Q_{app} according to the power law.

Figure 4.b shows the linear relationship between ln σ_P and 1000/T in order to calculate Q_{app} as Eq. 3 indicates. An average R^2 coefficient of 0.995 was obtained, evidencing that a single Q_{app} value can represent the experimental data (at least, at each strain rate). Considering n' = 2, an average Q_{app} value of 429.8 kJ·mol^{-1} was calculated. When GBS governs the deformation, Q_{app} corresponds either to the activation energy of grain boundary or of lattice diffusion (depending on which one of them controls it). Nevertheless, the evaluation of Q_{app} in the constitutive analysis of HEAs is still complex and unclear. Because of the compositional complexity of these alloys, there is usually no clear solute-solvent distinction, therefore is not easy to identify which elements play the main role in controlling the diffusion, indistinctly of the mechanism involved. In the present study, the obtained Q_{app} value is in the range of the self-diffusion activation energies of Mo or V [12]. Even though this would agree with the idea that lattice-controlled GBS is the governing deformation mechanism, an in-depth characterization of the microstructure and texture of the deformed samples is necessary to confirm it.

$$Q_{app} = Rn^{'}[\partial \ln \sigma_P / \partial(1/T)]_{\dot{\varepsilon}} \quad (3)$$

Lastly, Figure 5 illustrates the linear relationship between ln Z and ln σ_P. An elevated R^2 coefficient (0.993) was obtained, confirming the excellent agreement of the experimental data with the power law. Thus, a value of A' equals to $2.38 \cdot 10^9$ was calculated as the intercept of this curve. Therefore, the resulting relationship between Z and σ_P is represented in Eq. 4.

$$Z = \dot{\varepsilon} \exp(429.8/RT) = 2.38 \cdot 10^9 \, \sigma_P^2 \quad (4)$$

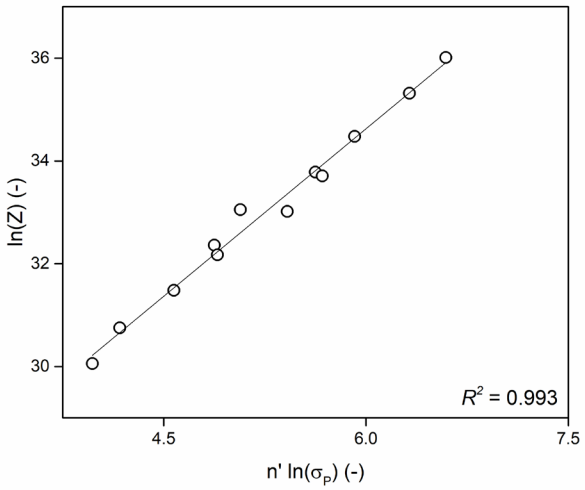

Figure 5: Plot used to the obtention of the value of A' and the corresponding R^2 coefficient of the power law.

On the other hand, Figure 6 illustrates the compression curves of R2AS and R2HT at 1000, 1050, and 1100 ºC employing a strain rate of 0.001 s^{-1}. As can be observed, the R2HT samples presented a considerably superior σ_P than the R2AS samples. Since the only considerable difference between R2AS and R2HT microstructures is the grain size of the constituents, this was attributed as the responsible of this superior mechanical behavior. Despite the increase in strength, R2HT samples still presented elevated ductility. These findings suggest that adjusting the microstructural features of PM RHEAs can result in an improvement in their high-temperature mechanical performance.

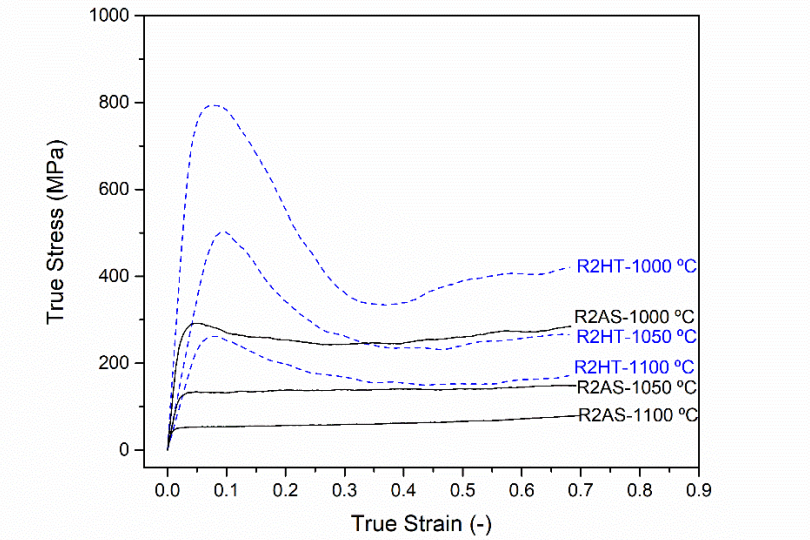

Figure 6: High-temperature compression curves of R2AS and R2HT samples, obtained using a strain rate of 10^{-3} s^{-1}.

Regarding the controlling deformation mechanism, two possibilities are on the table. Firstly, the R2AS and R2HT samples presented different deformation mechanisms, which would be responsible for this considerable difference. Senkov et al. [13] found that the strength remarkably dropped when GBS governs deformation; this agrees with the lower strength of the R2AS, which deformation is controlled by GBS according to the constitutive analysis. The second option is that GBS is also the controlling deformation mechanism of R2HT samples. This is plausible since GBS

is hindered by any condition that restricts the movement of grain boundaries, such as lower temperatures, higher strain rates, second phases in grain boundaries, and, as may be in the present case, coarser grain size; all these actions would produce an increase of the flow stress. Nevertheless, further microstructural analysis is required to determine the governing deformation mechanism.

Figure 7 illustrates the specific yield strength (SYS) of PM RHEAs, casting RHEAs, and the alloys of the present study. As can be observed, the R2AS alloy presented a considerably inferior SYS than the R2HT samples, increasing from 33 to 98 MPa/g·cm^{-3} at 1000 ºC. On the other hand, the alloys of the present study presented a poorer performance compared to $Al_xCrNbMoV$ (x = 0, 0.1, 0.5, and 1) RHEAs produced by MA+SPS [4,5], which ranges between 155 and 188 MPa/g·cm^{-3} at 1000 ºC. Nevertheless, except for the AlCrNbMoV alloy, none of them achieved a strain of 0.3, revealing that this superior strength was obtained by sacrificing their ductility. Apart from that, the SYS of the R2HT samples exceeds most of that of RHEAs that present considerable ductility at 1000 ºC.

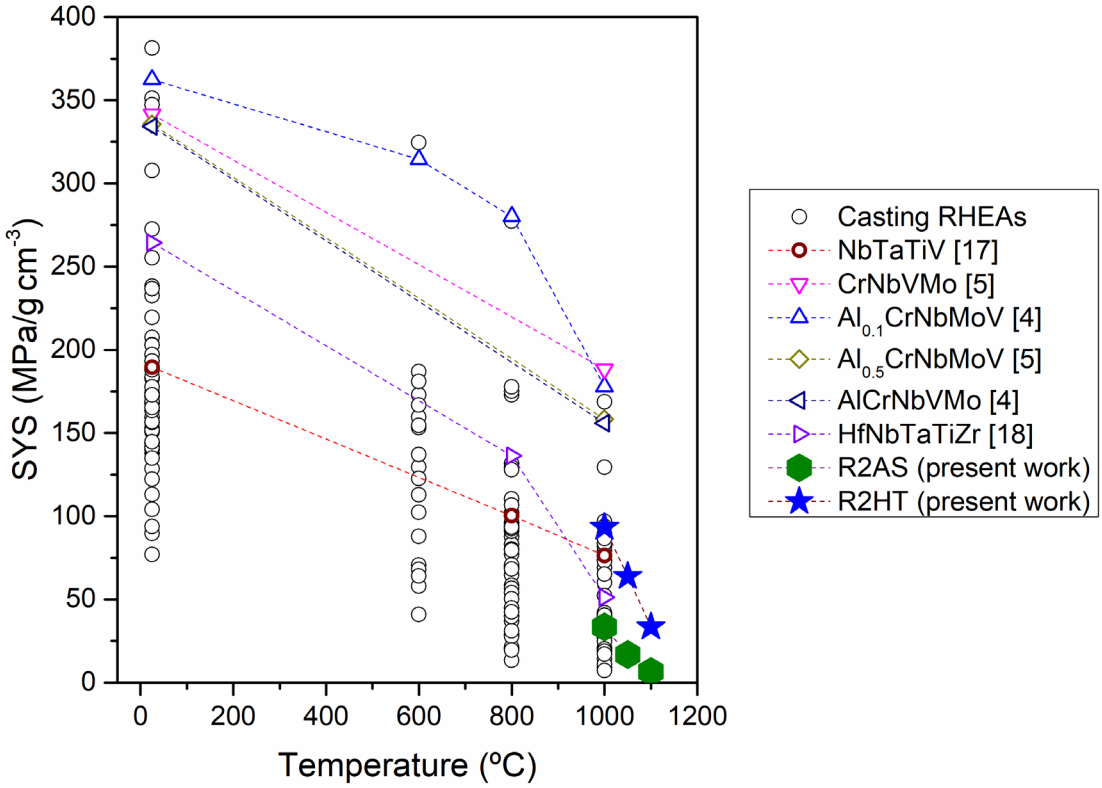

Figure 7: SYS of RHEAs produced by powder metallurgy [4,5,14,15], R2AS, R2HT, and casting RHEAs at different temperatures ($\dot{\varepsilon}$ = 0.001 s^{-1}).

Conclusions

The high-temperature compression tests of the R2 RHEA fabricated by powder metallurgy were effectively performed. Hence, the main conclusions of this work are:

i) A change in the mechanical behavior between 950 and 1000 ºC was observed that can be attributed to the precipitation of a phase, the dissolution of the Laves phase at high temperatures, or a change in the controlling deformation mechanism. Further studies are required to address this aspect.

ii) The expression $\dot{\varepsilon}\exp(429.8/RT) = 2.38 \cdot 10^9\ \sigma_P^2$ was obtained to model the σ_P in the studied temperature and strain rate range. An R^2 coefficient of 0.99 was obtained, evidencing the good agreement of the experimental data with the model.

iii) n' and Q_{app} values of 2 and 429.8 kJ·mol^{-1} were obtained with the conventional constitutive analysis considering the load partitioning effect produced by the presence of second phases. Hence, it was assumed that grain boundary sliding controlled the hot deformation of the alloy, while Q_{app} is in the range of the activation energies of self-diffusion of Mo and V.
iv) An increase of the grain size (from 0.35 to 1.2 μm in the case of the bcc phase) increased the strength while the ductility was not reduced. This can be attributed to a change in the controlling deformation mechanism, or well, that GBS is still the governing deformation mechanism but is hindered by the coarser grain size.

Acknowledgments
P. Martin gratefully acknowledges ANID/Doctorado Becas Chile/2019-72200338. JMC is grateful to the funding of project RTI2018-097885-B-C31 by the Agencia Estatal de Investigación (AEI) of Spain.

References

[1] O.N. Senkov, G.B. Wilks, D.B. Miracle, C.P. Chuang, P.K. Liaw, Intermetallics 18 (2010) 1758-1765. https://doi.org/10.1016/j.intermet.2010.05.014

[2] O.N. Senkov, G.B. Wilks, J.M. Scott, D.B. Miracle, Intermetallics 19 (2011) 698-706. https://doi.org/10.1016/j.intermet.2011.01.004

[3] O.N. Senkov, D.B. Miracle, K.J. Chaput, J.P. Couzinie, J. Mater. Res. 33 (2018) 3092-3128. https://doi.org/10.1557/jmr.2018.153

[4] B. Kang, J. Lee, H.J. Ryu, S.H. Hong, J. Alloys Compd. 767 (2018) 1012-1021. https://doi.org/10.1016/j.jallcom.2018.07.145

[5] B. Kang, T. Kong, H.J. Ryu, S.H. Hong, J. Mater. Sci. Technol. 69 (2021) 32-41. https://doi.org/10.1016/j.jmst.2020.07.012

[6] J. Pan, T. Dai, T. Lu, X. Ni, J. Dai, M. Li, Mater. Sci. Eng. A 738 (2018) 362-366. https://doi.org/10.1016/j.msea.2018.09.089

[7] B. Kang, J. Lee, H.J. Ryu, S.H. Hong, Mater. Sci. Eng. A 712 (2018) 616-624. https://doi.org/10.1016/j.msea.2017.12.021

[8] J.M. Cabrera, A. Al Omar, J.J. Jonas, J.M. Prado, Metall. Mater. Trans. A Phys. Metall. Mater. Sci. 28 (1997) 2233-2244. https://doi.org/10.1007/s11661-997-0181-8

[9] Q. Liu, G. Wang, Y. Liu, X. Sui, Y. Chen, S. Luo, Mater. Sci. Eng. A 809 (2021) 140922. https://doi.org/10.1016/j.msea.2021.140922

[10] R.R. Eleti, A.H. Chokshi, A. Shibata, N. Tsuji, Acta Mater. 183 (2020) 64-77. https://doi.org/10.1016/j.actamat.2019.11.001

[11] Z. Savaedi, R. Motallebi, H. Mirzadeh, J. Alloys Compd. 903 (2022) 163964. https://doi.org/10.1016/j.jallcom.2022.163964

[12] G. Neumann, C. Tuijn, Self-Diffusion and Impurity Diffusion in Pure Metals, First Edit, Elsevier Ltd., 2009. https://doi.org/10.1016/S1470-1804(08)00010-2

[13] O.N. Senkov, J.M. Scott, S. V. Senkova, F. Meisenkothen, D.B. Miracle, C.F. Woodward, J. Mater. Sci. 47 (2012) 4062-4074. https://doi.org/10.1007/s10853-012-6260-2

[14] A. Fu, W. Guo, B. Liu, Y. Cao, L. Xu, Q. Fang, H. Yang, Y. Liu, J. Alloys Compd. 815 (2020). https://doi.org/10.1016/j.jallcom.2019.152466

[15] X. Li, A. Fu, Y. Cao, S. Xu, S. Gao, J. Alloys Compd. 894 (2022). https://doi.org/10.1016/j.jallcom.2021.162414